

Geophysical Research Letters®



RESEARCH LETTER

10.1029/2023GL106990

Forecasting Tropical Annual Maximum Wet-Bulb Temperatures Months in Advance From the Current State of ENSO

Yi Zhang^{1,2,3} , William R. Boos^{1,4} , Isaac Held⁵, Christopher J. Paciorek⁶, and Stephan Fueglistaler^{4,7} 

¹Department of Earth and Planetary Science, University of California, Berkeley, CA, USA, ²Miller Institute for Basic Research in Science, University of California, Berkeley, CA, USA, ³Now at Courant Institute of Mathematical Sciences, New York University, New York, NY, USA, ⁴Climate and Ecosystem Sciences Division, Lawrence Berkeley National Laboratory, Berkeley, CA, USA, ⁵Program in Atmospheric and Oceanic Sciences, Princeton University, Princeton, NJ, USA, ⁶Department of Statistics, University of California, Berkeley, CA, USA, ⁷Department of Geosciences, Princeton University, Princeton, NJ, USA

Key Points:

- Tropical wet-bulb temperatures (TW) peak around 5 months after El Niño winters
- A multiple linear regression model considering the El Niño-Southern Oscillation index and the long-term warming trend effectively explains TW_{max} variability
- Our model quantifies the likelihood of strong El Niño and human-induced warming pushing TW_{max} to record-breaking levels

Supporting Information:

Supporting Information may be found in the online version of this article.

Correspondence to:

Y. Zhang,
yzhangaos@gmail.com

Citation:

Zhang, Y., Boos, W. R., Held, I., Paciorek, C. J., & Fueglistaler, S. (2024). Forecasting tropical annual maximum wet-bulb temperatures months in advance from the current state of ENSO. *Geophysical Research Letters*, 51, e2023GL106990. <https://doi.org/10.1029/2023GL106990>

Received 26 OCT 2023

Accepted 28 MAR 2024

Author Contributions:

Conceptualization: Yi Zhang, William R. Boos, Isaac Held, Stephan Fueglistaler

Data curation: Yi Zhang

Formal analysis: Yi Zhang

Funding acquisition:

Stephan Fueglistaler

Investigation: Yi Zhang

Methodology: Yi Zhang, Christopher

J. Paciorek

Validation: Yi Zhang, Christopher

J. Paciorek

Visualization: Yi Zhang

Writing – original draft: Yi Zhang

Writing – review & editing: William

R. Boos, Isaac Held, Christopher

J. Paciorek, Stephan Fueglistaler

Abstract Humid heatwaves, characterized by high temperature and humidity combinations, challenge tropical societies. Extreme wet-bulb temperatures (TW) over tropical land are coupled to the warmest sea surface temperatures by atmospheric convection and wave dynamics. Here, we harness this coupling for seasonal forecasts of the annual maximum of daily maximum TW (TW_{max}). We develop a multiple linear regression model that explains 80% of variance in tropical mean TW_{max} and significant regional TW_{max} variances. The model considers warming trends and El Niño and Southern Oscillation indices. Looking ahead, the strong-to-very-strong El Niño at the end of 2023, with an Oceanic Niño Index of ~ 2.0 , suggests a 2024 tropical land mean TW_{max} of 26.2°C (25.9–26.4°C), and a 68% chance (24%–94%) of breaking existing records. This method also predicts regional TW_{max} in specific areas.

Plain Language Summary The heat and humidity in the tropics can be particularly challenging for people to stay comfortable and healthy. This combination of heat and moisture is described using a measure called the wet-bulb temperature (TW). We found that these extremely humid and hot conditions on land can be predicted about 5 months in advance using a physics-based statistical model. The forecast is possible because the peak of El Niño comes before the peak in the warmest sea surface temperatures, which affects the maximum TW on land. This prediction can help tropical societies to better prepare for extreme heat.

1. Introduction

The tropics, characterized by high temperatures and humidities, face heightened risks from heat-related impacts (Parkes et al., 2022; Raymond et al., 2020, 2021; Sherwood & Huber, 2010). This vulnerability is exacerbated by the consistent warming trend, leading to more frequent and intense heat events. Superimposed on the warming trend is the El Niño-Southern Oscillation (ENSO). El Niño events, typified by warmer central and eastern equatorial Pacific Ocean temperatures, trigger shifts in atmospheric circulation that modify global temperature and precipitation patterns (Yulaeva & Wallace, 1994). These events often result in more frequent and intense heatwaves in many regions, including the tropics (Arblaster & Alexander, 2012; Revadekar et al., 2009; Thirumalai et al., 2017). In contrast, La Niña events, marked by cooler Pacific Ocean temperatures, tend to bring cooler and wetter conditions. In light of ongoing global warming, an El Niño event superimposed on the current warming could result in unparalleled hot weather, underscoring the need for further investigation and preparedness.

The physical mechanism underlying pan-tropical land warming during El Niño years is the free-tropospheric heating that arises from deep convection over anomalously warm sea surface temperatures (SSTs). This heating causes atmospheric columns over remote land to adjust to a warmer state in response to the elevated free troposphere temperatures (Brown & Bretherton, 1997; Chiang & Sobel, 2002). Notably, this free-tropospheric warming occurs a few months after peak El Niños (Chiang & Sobel, 2002; Pan & Oort, 1983; Sobel et al., 2002), as the SSTs in convective regions (the warmer portions of tropical SSTs) take a few months to warm following peak El Niño events as a result of the interactions within the coupled air-sea system (Fueglistaler, 2019; Hogikyan et al., 2022; Klein et al., 1999; Su et al., 2005; Xie et al., 2009).

© 2024. The Authors.

This is an open access article under the terms of the [Creative Commons Attribution License](https://creativecommons.org/licenses/by/4.0/), which permits use, distribution and reproduction in any medium, provided the original work is properly cited.

As recognition of humid heat's importance grows, the effects of global warming and ENSO on extreme humid heat, in addition to extreme temperatures, are emerging as active areas of research. Anthropogenic warming is a primary driver of tropical increases in wet-bulb temperature (TW), a common measure of humid heat (Buzan & Huber, 2020; Sherwood & Huber, 2010; Zhang et al., 2021). Zhang et al. (2021) shows that tropical TW is also controlled by the mechanism described above, namely that extreme TW over tropical land is limited by the near-uniform free-tropospheric temperature which is set by the warmest SSTs. According to Zhang et al. (2021), extreme TW in the tropics is projected to rise by 1°C for every 1°C increase in tropical mean warming. Concurrently, ENSO variability can significantly impact TW patterns over shorter timeframes (Ivanovich et al., 2022; Rogers et al., 2021; Speizer et al., 2022). Research has highlighted anomalously high tropical land mean TW associated with the 1997–1998 El Niño (Raymond et al., 2020; Zhang et al., 2021), as well as the more frequent occurrence of regional extreme TW during El Niño years (Rogers et al., 2021; Speizer et al., 2022).

In this study, we draw upon existing knowledge that (a) maximum wet-bulb temperatures (TW_{\max}) over land are influenced by the warmest SSTs in the tropics, and (b) a lag of about 4 months occurs in the warming of the warmest SSTs after a peak El Niño event. We aim to construct a predictive model for extreme TW that can provide early warning of extreme TW_{\max} levels several months in advance. We then explore the regional validity of this model and focus on a few high-TW zones where the model is effective. While earlier research has studied the delayed effects of El Niño on the following summer in Asia, known as the “Indian Ocean capacitor effect” (Xie et al., 2009), our focus extends to extreme TW in all tropical land areas. Our research aims to enhance seasonal predictions of extreme TW in the tropics, offering more accurate climate risk assessments and enhancing preparedness efforts in these regions.

2. Data and Methods

2.1. Wet-Bulb Temperature

Wet-bulb temperatures (TW) are calculated using the ERA5 hourly reanalysis product (Hersbach et al., 2020) by solving the following equation:

$$c_p T_s + L_v q_s = c_p TW + L_v q_{\text{sat}}(TW), \quad (1)$$

where T_s and q_s represent the 2-m temperature and 2-m specific humidity, respectively. L_v denotes the latent heat of vapourization, and c_p represents the specific heat capacity of air at constant pressure. In our computations, we use c_p as 1004.7090 J/kg/K and L_v as 2.5008×10^3 J/kg. Although neglecting the temperature dependence of c_p and L_v introduces a small error in TW, it is sufficient for our purposes.

Since the ERA5 data set does not directly provide the 2-m specific humidity, we calculate it using the hourly 2-m dewpoint temperature (T_d) and surface pressure (p_s), considering the molecular mass ratio of water vapor and air (ϵ) of 0.621,981. The specific humidity (q_s) is determined as follows:

$$q_s = \frac{\epsilon e_{\text{sat}}(T_d)}{p_s - (1 - \epsilon)e_{\text{sat}}(T_d)}, \quad (2)$$

where e_{sat} represents the saturation vapor pressure calculated using the Clausius-Clapeyron equation, specifically the Tetens's formula, consistent with the methodology of the European Center for Medium-Range Weather Forecasts (ECMWF) (ECMWF, 2014):

$$e_{\text{sat}} = a_1 e^{\frac{a_2(T - T_0)}{T - a_3}}, \quad (3)$$

with the parameter values for saturation over water: $a_1 = 611.21$ Pa, $a_2 = 17.502$, $a_3 = 32.19$ K, and $T_0 = 273.15$ K.

To focus on extreme TW values, we consider the daily maximum TW and then determine the annual maximum, denoting it as TW_{\max} .

2.2. ENSO Index

The strength of the El Niño-Southern Oscillation (ENSO) phenomenon is assessed using the Oceanic Niño Index (ONI), which serves as National Oceanic and Atmospheric Administration (NOAA)'s primary index for monitoring the oceanic component of ENSO. The ONI is calculated as the rolling 3-month average temperature anomaly, from the long-term average, of the surface of the east-central tropical Pacific near the International Dateline in the Niño 3.4 region (5°N–5°S, 120°–170°W). This ONI data set is based on NOAA Extended Reconstructed Sea Surface Temperature (ERSST) Version 5.

3. Results

3.1. ONI Leads TW_{\max} by Months

To demonstrate that warm tropical SSTs control extreme TW over land through the mediation of the free tropospheric temperature, we show the time series of these three variables in Figure 1a. All time series are presented as running means of 6 months with the monthly climatology removed. The anomalies in the free-tropospheric temperature at the 500-hPa level (T_{500}) is divided by 1.4, because a 1-K increase in SST would result in about 1.4 K of increase in T_{500} following a moist adiabatic lapse rate. The tropical land-average of monthly maximum TW exhibits a notable long-term warming trend of approximately 0.2 K per decade from 1979 to 2022, accompanied by significant interannual variability. The monthly average 500-hPa temperature (\overline{T}_{500}) and the top 25% of monthly mean SST ($SST_{25\%}$) show similar interannual variabilities and long term trends as TW, with contemporaneous peaks. These findings support the notion put forward by Zhang et al. (2021) that the warmest SSTs control the maximum TW over land, with the coupling occurring rapidly enough to render the maximum TW and $SST_{25\%}$ variations appear nearly simultaneous in monthly data.

To predict extreme TW over land, we turn our attention to the predictors for the warmest 25% of SSTs. ENSO induces significant shifts in atmosphere-ocean circulations, altering the energy budget of the ocean's mixed layer and influencing the relatively warm SSTs that lie in regions of deep atmospheric convection. The interannual variability in $SST_{25\%}$ closely resembles that in the Oceanic Niño Index (ONI), which does not exhibit a long-term trend by design. Moreover, major El Niño events coincide with pronounced spikes in $SST_{25\%}$ and TW_{\max} anomalies, with the latter two typically occurring with a lag of approximately 4 months. Notably, the warming of TW_{\max} during the developing phase of the 1991–1992 El Niño was interrupted by the aerosol cooling effect of the Mt. Pinatubo eruption in June 1991, leading to a missed peak in TW_{\max} despite rising ONI. Another significant volcanic eruption, El Chichón in 1982, also coincided with an El Niño event. Although elevated TW_{\max} values still occurred, they were partially offset by volcanic cooling, and the peak TW_{\max} lagged the ONI peak by 9 months. Excluding the volcanic eruptions, other major El Niño events consistently precede anomalous high $SST_{25\%}$ values and, consequently, extreme TW_{\max} values. These findings suggest the potential to use the ONI to statistically predict TW_{\max} some months later, perhaps even in the following year.

3.2. Multiple Linear Regression Model of TW_{\max}

We develop a multiple linear regression model to predict the annual maximum of daily maximum wet-bulb temperature (TW_{\max}) using two independent variables: a year variable to account for the warming trend and the Oceanic Niño index (ONI) to represent ENSO. The objective is to explain anomalies in TW_{\max} as a linear combination of a constantly rising baseline and the ONI from a specific month of the preceding year:

$$TW_{\max,t} = \beta_0 + \beta_1 t + \beta_2 ONI_{m,t-1} + \epsilon_t \quad (4)$$

Initially, we examine whether this model can capture the tropical land average values of TW_{\max} between 30°S and 30°N. Even though the exogenous variable is an annual maximum, the process of spatial averaging yields an error term with a near-Gaussian distribution, justifying the use of multiple linear regression analysis. We compute the R^2 values for different months (m) in the model using the tropical land average of TW_{\max} from 1980 to 2022, with the year t and ONI from 1979 to 2021 as the independent variables (Figure 1b). The highest R^2 value of 0.764 is obtained when using the ONI from all Novembers to predict the land-mean TW_{\max} in the following years. However, considering the impact of major volcanic eruptions on TW_{\max} , we exclude the years affected by these eruptions to enhance the accuracy of the linear regression model. We exclude TW_{\max} for the 2 years following the

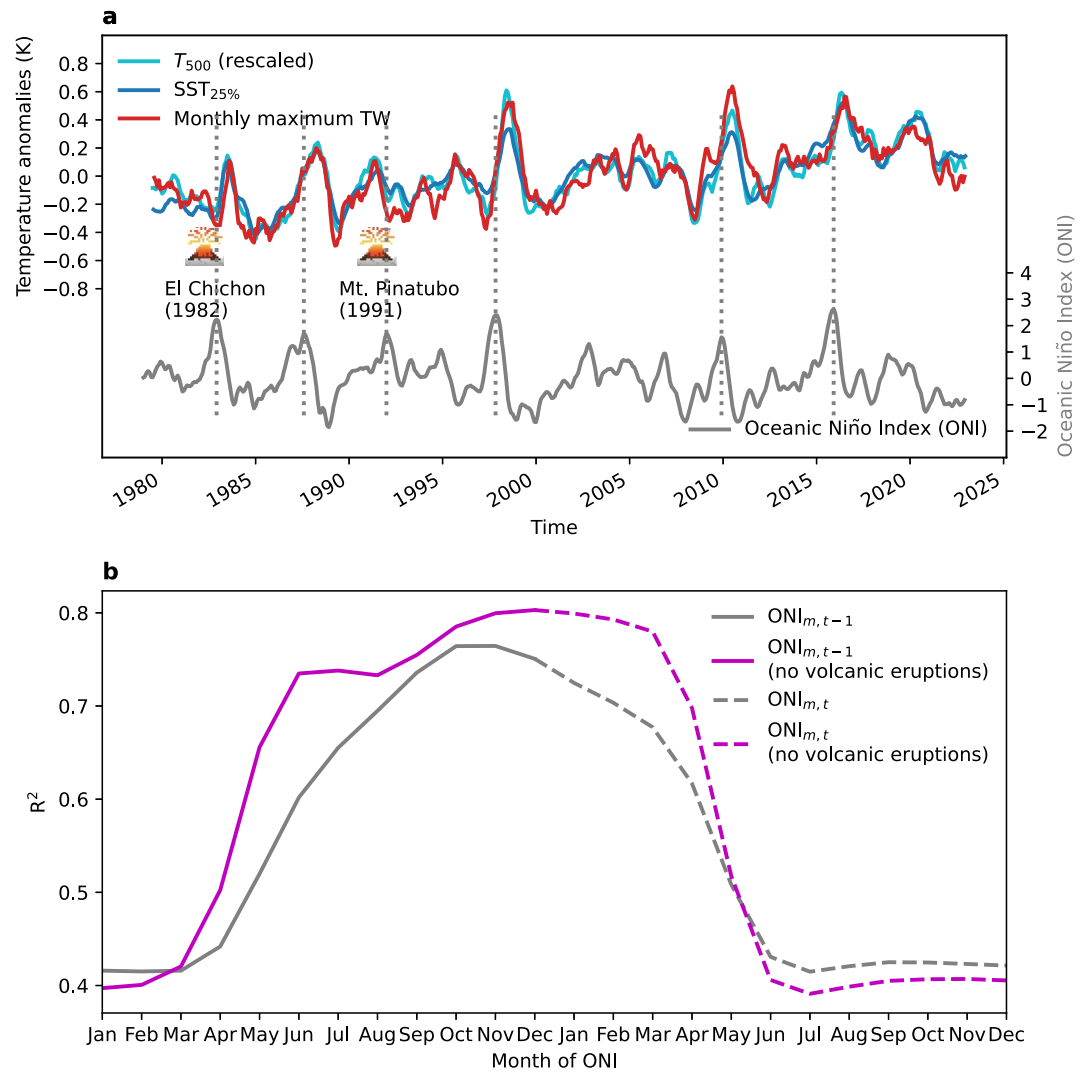


Figure 1. El Niño-Southern Oscillation variability leads tropical land TW_{max} by a few months. a, Monthly anomalies of tropical (between $30^{\circ}S$ and $30^{\circ}N$) land mean TW_{max} (red), the upper-quartile-mean sea surface temperature (blue) from Hadley Center Sea Ice and SST data set (Rayner et al., 2003), and the average 500-hPa temperature divided by the moist adiabatic amplification factor 1.4 (cyan), as well as the Oceanic Niño Index (ONI) in gray. Timing of strong El Niños (ONI > 1.5) are marked with vertical dotted lines. b, R^2 values of the multiple linear regression model specified in Equation 4 using ONI from January to December of preceding years (solid) and contemporaneous years (dashed). The gray line shows the fit using all 43 years between 1990 and 2022, while the magenta line shows the fit of 39 years to exclude major volcanic eruptions.

Mt. Pinatubo eruption (1992 and 1993) and the two years following the El Chichón eruption (1983 and 1984). Consequently, we discard ONI values from 1982, 1983, 1991, and 1992. The performance of the regression improves, with the highest R^2 value of 0.803 achieved using December ONI from the preceding year. Notably, the R^2 values exhibit substantial increases from April to August, reaching a relatively high value of 0.735 in June. This aligns with the spring predictability barrier (e.g., Webster and Yang (1992)) and suggests that a skillful prediction for TW_{max} in the subsequent year might be obtained as early as June of the current year.

For completeness we also show the R^2 values using ONI for each month of the same year as the TW_{max} in Figure 1b. The explained variance does not increase when using ONI of the same year as the occurrence of TW_{max} . This is because TW_{max} over land is not constrained by the contemporaneous ONI but rather the warmest SSTs which lag ONI by a few months.

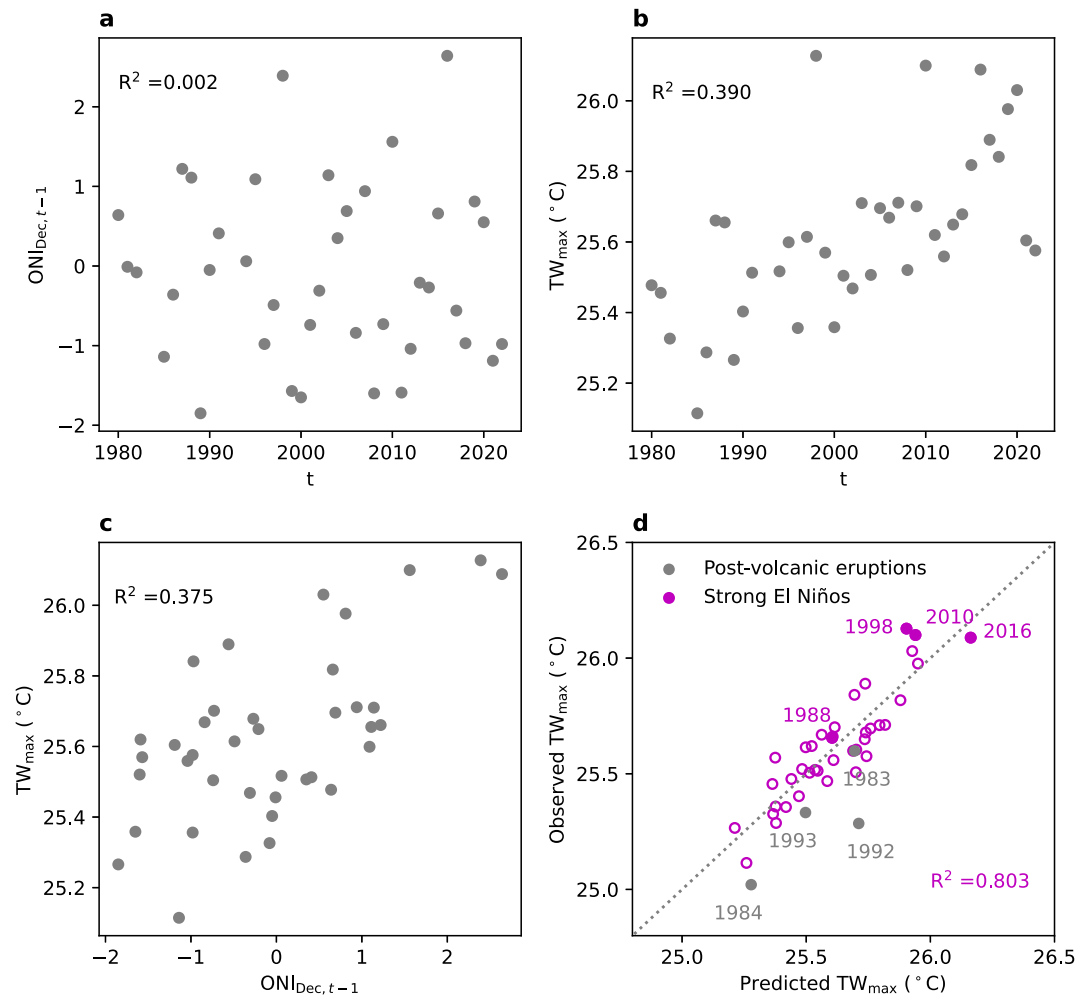


Figure 2. Visualization of the multiple linear regression for 30°S–30°N land-mean temperature (TW_{max}). a, Scatter plot of independent variables—December ONI of preceding years ($ONI_{Dec,t-1}$) and year (t). b, Scatter plot of 30°S–30°N land-mean TW_{max} and year (t). c, Scatter plot of 30°S–30°N land-mean TW_{max} and $ONI_{Dec,t-1}$. d, TW_{max} from ERA5 versus the predicted TW_{max} by the regression model. Years following major volcanic eruptions are excluded from the fit and are plotted separately in gray. Years after strong El Niños are highlighted. The gray dotted line indicates 1/1.

Figure 2 illustrates the multiple linear regression model in Equation 4 when m is December. There is negligible multicollinearity between the two independent variables (Figure 2a), year (t) and ONI of the preceding December ($ONI_{Dec,t-1}$). Each independent variable alone explains slightly less than 40% of variance in the tropical mean TW_{max} . Figure 2d shows the observed versus the model-predicted TW_{max} with 80% of variance explained. The performance of the model is roughly constant across all years and does not depend on strong signals from major El Niños.

In the following, we progressively apply the model to zonal-mean and grid-point-level TW_{max} . TW undergoes a strong annual cycle mainly driven by local insolation, while the warmest quartile of SSTs ($SST_{25\%}$ hereafter) limits peak TW values across tropical locations with a comparatively smaller seasonal cycle; there is less than 1 K difference between the warmest and the coldest months of a year for $SST_{25\%}$, whereas TW can vary by 10 K over many locations. ENSO variability and an upward trend are present in $SST_{25\%}$ throughout the year (Figure S7 in Supporting Information S1), therefore the model is potentially effective for local TW_{max} regardless of the month of occurrence. Given the performance of December ONI for the tropical mean TW_{max} (Figure 1b) and the zonal-mean TW_{max} over most latitudes (Figure S3 in Supporting Information S1), all regional regressions in the rest of the paper are against December ONI with the four years affected by volcanism removed between 1980 and 2022, resulting in 39 data points and two independent variables. Note that the ONI is a 3-month running mean, therefore

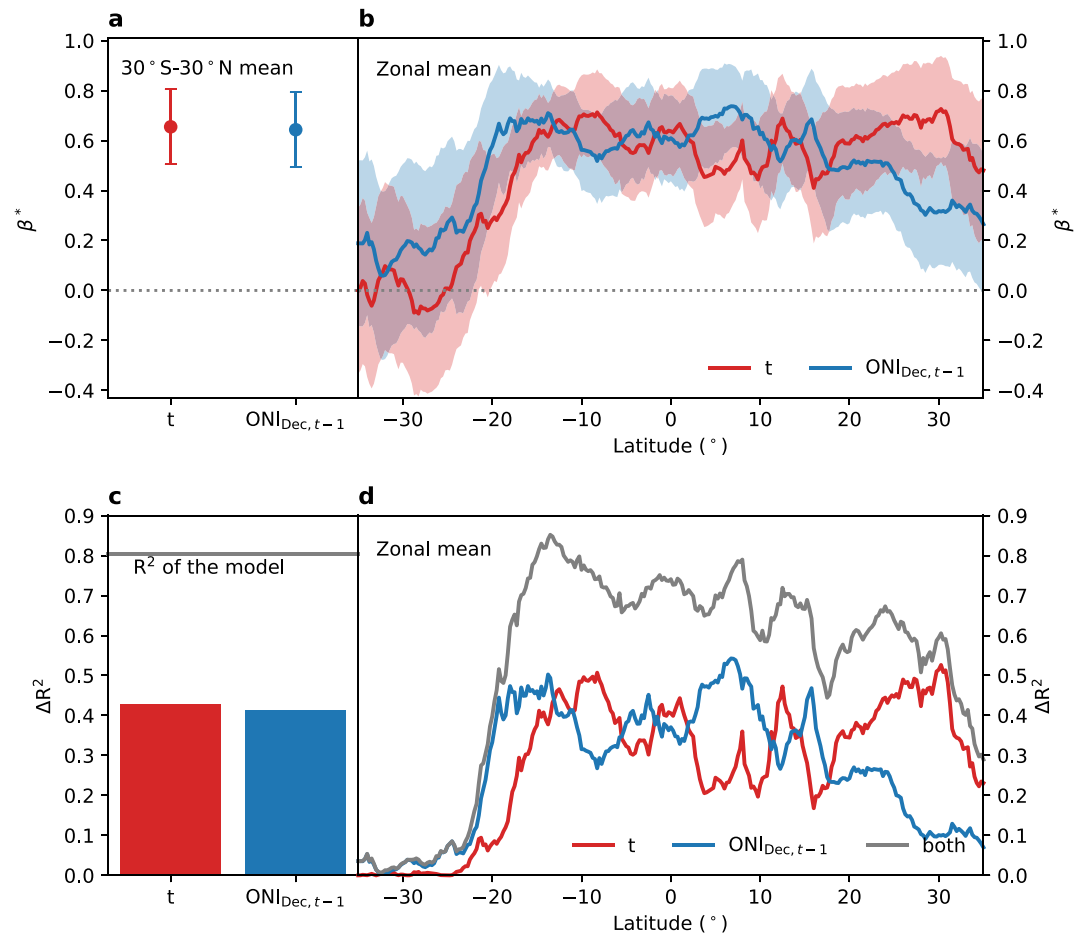


Figure 3. Relative importance of constant warming and El Niño-Southern Oscillation variability in explaining temperature (TW_{\max}) variability. a, Standardized regression coefficients ($\hat{\beta}^*$) and the 95% confidence intervals for both independent variables. b, Same as a but for zonal mean TW_{\max} over land. c and d, Incremental R^2 (ΔR^2) for each independent variable, estimated by removing each variable from the full regression, and the R^2 of the full model (gray).

December ONI values contain information from January of the following years; however, TW_{\max} occurs in January primarily for some land regions south of 15°S (Figure S5 in Supporting Information S1), and we later demonstrate predictive skill of the model 3–7 months in advance for sample regions near the equator or in the Northern subtropics.

3.3. Impact of Warming Trend and ENSO Variability on TW_{\max}

To assess the relative contributions of warming and ENSO to explaining the variance in TW_{\max} , we estimate the standardized regression coefficients ($\hat{\beta}^*$) by carrying out the multiple linear regression on standardized variables, with the standardization following $\frac{x-\bar{x}}{s_x}$ where \bar{x} denotes the average and s_x the standard deviation. The standardized regression coefficients provide the change in the dependent variable per one-unit change in the independent variable measured in standard deviations. $\hat{\beta}^*$ would equal the correlation between the respective independent variable and TW_{\max} if the independent variables were uncorrelated. The 95% confidence intervals of $\hat{\beta}^*$ for the warming trend and ENSO variability are 0.65 ± 0.15 and 0.64 ± 0.15 , indicating that both factors contribute similarly to the variance of the tropical land mean TW_{\max} (Figure 3a).

To examine the spatial distribution of these coefficients, we compute $\hat{\beta}^*$ by regressing the standardized zonal land mean TW_{\max} (i.e., TW_{\max} at each grid point zonally averaged over land only) against the same two standardized independent variables.

Figure 3b illustrates the estimated β^* as a function of latitude. Over most latitudes in the tropics, the 95% confidence intervals of $\hat{\beta}_1^*$ (warming) and $\hat{\beta}_2^*$ (ENSO) strongly overlap, suggesting a similar contribution at each latitude. However, in the southern subtropics, the magnitude of $\hat{\beta}^*$ values for both variables declines, and the 95% confidence interval encompasses 0 south of 20°S, indicating that the regression model is not useful in these latitudes. Notably, warming exerts a stronger influence on the northern subtropics compared to ENSO.

The implications of a one-standard-deviation change may differ when the independent variables follow different distributions, as is the case here with the uniformly distributed t variable and the approximately normally distributed ONI. To provide further evidence and a complementary perspective, we employ an alternative approach by calculating the increment in R^2 (ΔR^2) for each variable:

$$\Delta R_i^2 = R_{\text{full}}^2 - R_{\text{Reduced},i}^2, \quad (5)$$

where R_{full}^2 represents the R^2 value of the full model (Equation 4), and $R_{\text{Reduced},i}^2$ corresponds to the R^2 value when the i th independent variable is removed from the regression model. ΔR_i^2 can be loosely regarded as the contribution of the i th variable to the full model. This method yields similar results (Figures 3c and 3d), with warming contributing 0.428 and ENSO contributing 0.413 for the tropical mean TW_{max} . The latitudinal patterns of the relative magnitudes of ΔR^2 values closely resemble those of $\hat{\beta}^*$. Furthermore, the R^2 value of the full model indicates that the model performs best in the deep tropics, consistent with empirical findings that support the validity of the convective quasi-equilibrium and weak-temperature-gradient assumptions in that latitudinal range (Chiang & Lintner, 2005; Held & Hou, 1980; Zhang & Fueglistaler, 2020).

3.4. Regional Regression

When evaluating the model's performance for gridbox-level annual maxima, the assumption of a Gaussian error term in Equation 4 becomes less appropriate. In this context, we assume a generalized extreme value (GEV) distribution for the error term and determine the parameters through maximum likelihood estimation (Text S1 in Supporting Information S1).

The model's performance exhibits a spatial pattern consistent with the zonal-mean analysis discussed above, with its lowest RMSE values in the deep tropics and an increase toward higher latitudes (Figure 4a).

The $\hat{\beta}$ values for both warming (Figure 4b) and ENSO (Figure 4c) are comparable in magnitude when multiplied by the standard deviations of the respective independent variable, implying their similar impacts on TW_{max} variability across different locations. Contrary to expectations that TW_{max} in all tropical land is constrained by the warmest SSTs irrespective of place, the coefficient for warming ($\hat{\beta}_1$; Figure 4b) exhibits notable spatial variations. In contrast, the ENSO coefficient ($\hat{\beta}_2$; Figure 4c) is relatively uniform, with El Niños leading to higher TW_{max} in the following years across most regions. This suggests that, despite El Niño's inherent spatial characteristics, its occurrence induces a relatively uniform response in the following year's continental TW_{max} .

There are two potential causes of the spatial pattern in the coefficient of warming ($\hat{\beta}_1$): the influence of local land surface conditions, and the uneven response of free-tropospheric temperatures to localized convective heating (Gill, 1980; Matsuno, 1966). Further analysis suggests that the former is more likely (Text S2 in Supporting Information S1), as evidenced by the fact that the areas of negative $\hat{\beta}_1$ coincide with regions of strongly negative trends in the annual-mean 2-m specific humidity (q_s ; Figure S1b in Supporting Information S1). Such drying trends could stem from land use change, a process not explored in this study. A drier land surface deepens the planetary boundary layer, distributing surface heat fluxes within a deeper layer and enhancing entrainment of dry free tropospheric air; both of these processes lead to lower boundary layer moist static energy and surface TW (Kong & Huber, 2023; Pal & Eltahir, 2001).

The above analyses illustrate the spatial heterogeneity in the relationships of TW_{max} with warming and ENSO. While it is reasonably true that tropical TW_{max} increases over land are uniformly limited by the warmest sea surface temperatures (Zhang et al., 2021), the regional disparities highlight the limitation of this assumption. These results emphasize the importance of conducting localized assessments, which we do next.

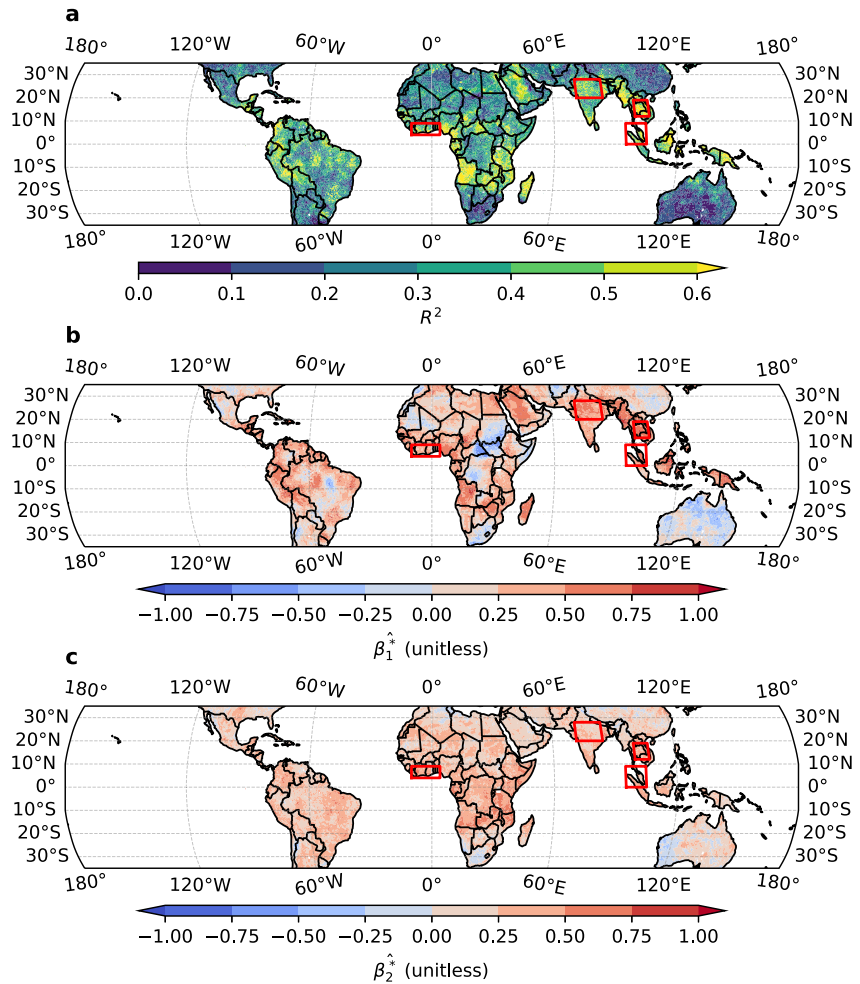


Figure 4. Results of fitting the model in Equation 4 at each location assuming generalized extreme value distributions of the error terms. a, R^2 , defined as the regression sum of squares divided by the total sum of squares. Red boxes outline regions of interest further analyzed in Figure 5 b, Standardized regression coefficient of warming. c, Standardized regression coefficient of El Niño-Southern Oscillation variability.

We have chosen four regions (marked as red boxes in Figure 4a) to assess how the model in Equation 4 predicts regional-mean TW_{\max} . The choice of these regions is not governed by any strict rule, but we generally pick regions that exhibit relatively high values in climatological TW_{\max} (Figure S4a in Supporting Information S1) and population density (Figure S4b in Supporting Information S1), and relatively low values in RMSE (Figure 4a). Spatial averaging produces error terms approximating Gaussian distributions, justifying the suitability of applying the multiple linear regression analysis. The model's performance in these smaller regions is depicted in Figures 5b–5d, while Figure 5a illustrates the same for the tropical land mean. The model effectively explains TW_{\max} variability at both regional and tropical mean scales. The contributions of warming and ENSO exhibit regional variations, as evidenced by the range of ΔR^2 values in Table 1. In Southeast Asia, for instance, the variability of TW_{\max} is predominantly influenced by the warming trend, with higher TW_{\max} values occurring in more recent years (Figure 5c). Conversely, the Sahel region exhibits stronger sensitivity to ENSO variability, with 1998 and 2016 having the highest TW_{\max} (Figure 5b).

TW_{\max} occur at different times of year in different regions. A general pattern emerges, with TW_{\max} events occurring during boreal summer (June–August) north of 15°N, boreal winter (December–February) south of 15°S, and boreal spring (March–May) and fall (September–November) between 15°S and 15°N (Figure S5a in Supporting Information S1). For the four selected regions, TW_{\max} typically occurs in April for Sahel, May for Southeast Asia and Sumatra, and June to August for North India (Figure S5b in Supporting Information S1). The

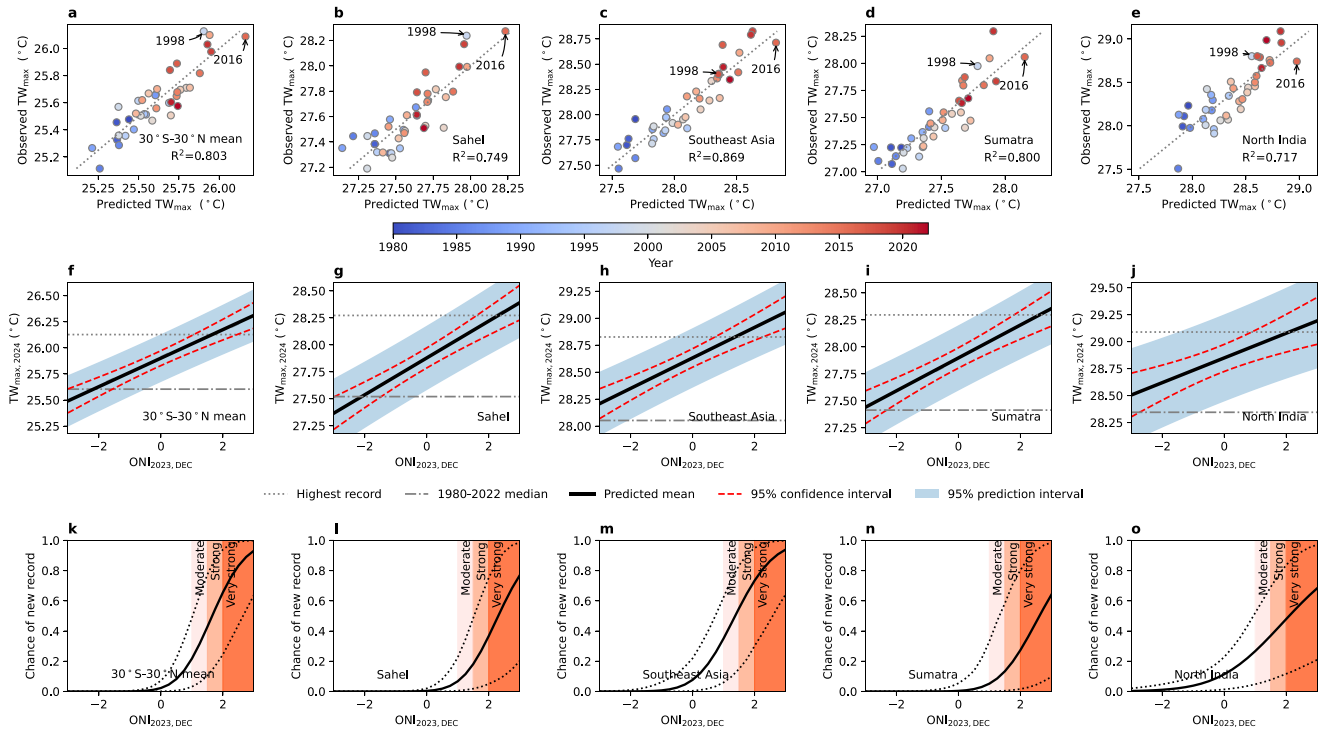


Figure 5. Example temperature (TW_{max}) forecast for 2024. a-e, Performance of multiple linear regression for 30°S–30°N land mean and four regions marked in Figure 4a. Color indicates the year of the data point. Two major El Niños-1998 and 2016-are highlighted. f-j, Predicted $TW_{max, 2024}$ as a function of December Oceanic Niño Index (ONI), 2023. Confidence intervals in red account for the standard error of the predicted mean. Prediction intervals in blue additionally take into account the year-to-year variability around the predicted mean. k-o, Estimated chance of TW_{max} setting new records in 2024 in the tropical mean and each region conditioned upon the strength of El Niño by the end of 2023. ONI ranges of moderate ($1.0 \leq ONI < 1.5$), strong ($1.5 \leq ONI < 2.0$) and very strong ($ONI \geq 2.0$) El Niño events are marked.

Table 1
Summary of Multiple Linear Regression Results^a

Region	30°S–30°N mean	Sahel	Southeast Asia	Sumatra	North India
$\hat{\beta}_1$ (°C/year)	0.0125 ± 0.0029^b	0.0121 ± 0.0037	0.0235 ± 0.0034	0.0184 ± 0.0038	0.0218 ± 0.0050
$\hat{\beta}_2$ (°C/unit ONI)	0.137 ± 0.032	0.171 ± 0.042	0.141 ± 0.038	0.152 ± 0.042	0.115 ± 0.056
$\hat{\beta}_1^*$ (standardized $\hat{\beta}_1$)	0.65	0.55	0.84	0.73	0.78
$\hat{\beta}_2^*$ (standardized $\hat{\beta}_2$)	0.64	0.70	0.45	0.55	0.37
ΔR_1^2	0.428	0.300	0.700	0.538	0.607
ΔR_2^2	0.413	0.483	0.203	0.298	0.135
R^2	0.803	0.749	0.869	0.800	0.716
F-statistic, $P > F$	73.36, $2.0e-13$	53.66, $1.6e-11$	119.3, $1.3e-16$	72.04, $2.6e-13$	45.50, $1.4e-10$
t, $P > t $ for $\hat{\beta}_1$	8.844, $1.5e-10$	6.557, $1.3e-07$	13.859, $5.3e-16$	9.843, $9.5e-12$	8.783, $1.8e-10$
t, $P > t $ for $\hat{\beta}_2$	8.686, $2.3e-10$	8.321, $6.6e-10$	7.465, $8.1e-9$	7.328, $1.2e-8$	4.134, $2.0e-4$
Root Mean squared error (RMSE; °C) ^c	0.103	0.134	0.124	0.136	0.182
Leave-one-out cross-validation RMSE (°C)	0.113 (+9.45% ^d)	0.147 (+9.17%)	0.135 (+8.86%)	0.149 (+9.05%)	0.199 (+9.71%)
Walk-forward validation RMSE (°C)	0.119 (+7.08% ^e)	0.138 (+20.1%)	0.156 (+17.6%)	0.171 (+18.8%)	0.194 (+17.6%)
Record-setting probability (ONI = 1.5)	42% (11%–78% ^f)	15% (1.8%–49%)	56% (15%–84%)	11% (0.5%–58%)	35% (7.7%–69%)
Record-setting probability (ONI = 2.64)	90% (50%–99.5%)	66% (14%–95%)	92% (55%–99.5%)	51% (5.5%–95%)	63% (17%–94%)

^aNumber of Observations: 39; Residuals degree of freedom: 36; Model degree of freedom: 3. ^b95% confidence interval. ^cMaximum likelihood estimate of MSE, not the unbiased MSE. ^dPercentage change compared to the regression model with all 39 data points. ^ePercentage change of RMSE of the last 19 data points. ^f95% BCa bootstrap interval.

multiple linear regression model thus demonstrates an average lead time of approximately 5 months for tropical land areas and a range of three to 7 months for the four regions of interest.

3.5. Forecasting TW_{\max} Months in Advance

Before making predictions with the multiple linear regression model, we assess its predictive skill using leave-one-out cross-validation and walk-forward validation which is more suitable for time series data. This is motivated by the possibility of overfitting, especially since our model was trained using the full data set. The moderate increases in RMSE during cross-validation (Table 1) suggest that the model is not seriously overfitted and is suitable for making predictions with details provided in Text S3 and Figures S6 in Supporting Information S1.

Our objective is to generate a forecast of TW_{\max} for the upcoming year based on the December Oceanic Niño Index (ONI) of the current year. Note that the ONI is a 3-month running mean, with December ONI of the current year technically containing information from January of the upcoming year, but nearly all land north of 15°S has TW_{\max} occurring in March or later of the upcoming year (Figure S5b in Supporting Information S1). Taking the year 2024 as an example, the predicted mean depends on $ONI_{Dec,2023}$ following:

$$\widehat{TW}_{\max,2024} = \widehat{\beta}_0 + 2024\widehat{\beta}_1 + \widehat{\beta}_2 ONI_{Dec,2023}. \quad (6)$$

Figures 5e–5h presents the 95% confidence intervals of the predicted mean and the 95% prediction intervals of $TW_{\max,2024}$ as a function of $ONI_{Dec,2023}$ (Text S4 in Supporting Information S1). As expected, even in a neutral ENSO state, the mean predicted $TW_{\max,2024}$ values in all four regions (Figures 5f–5h) as well as the tropical mean (Figure 5e) surpass the median of past records. This demonstrates the influence of the cumulative warming at the present level on TW_{\max} . A rough estimate of the impact of warming since 1980 on TW_{\max} is the number of years (44 years) multiplied by $\widehat{\beta}_1$, yielding 0.55 K for the tropical mean. The ONI value required to achieve a comparable effect can be estimated by dividing the warming-induced increase in TW_{\max} by $\widehat{\beta}_2$. Remarkably, an ONI value of 4.0, representing a super El Niño of unprecedented magnitude, would be necessary to match the increase in tropical mean TW_{\max} caused by cumulative warming. Although this estimation is not rigorous, it provides an estimate of the magnitude of the cumulative warming effect since 1980, equivalent to an exceptionally strong El Niño.

Next, we estimate the probability of a new TW_{\max} record being set in 2024, assuming knowledge of $ONI_{Dec,2023}$. Rigorously estimating this probability is challenging, and our estimate is contingent upon certain assumptions. We assume that the predicted TW_{\max} at each $\mathbf{x}_p = (1, 2024, ONI_{Dec,2023})^T$ follows a Gaussian distribution centering at the predicted mean given by Equation 6 with a standard deviation equaling the root mean squared error (RMSE; we use the maximum likelihood estimate of RMSE rather than the unbiased estimate). For each $ONI_{Dec,2023}$ value, we then compute the area under this Gaussian distribution when the predicted TW_{\max} exceeds the highest record, resulting in the central estimates of the probability of a new TW_{\max} record being set (solid lines in Figures 5i–5l). The 95% confidence intervals for this probability, shown as dotted lines in Figures 5i–5l, were derived using the bias-corrected and accelerated (BCa) bootstrap method (Text S5 in Supporting Information S1).

For the tropical mean TW_{\max} , an Oceanic Niño Index (ONI) of 1.5 by the end of 2023 leads to a central estimate of a 42% probability of surpassing the TW_{\max} record in 2024 with the 95% confidence interval ranging from 11% to 78% (Figure 5k). In contrast, if an El Niño as intense as the 2015/2016 event (with an ONI of 2.64) occurs, the central probability estimate increases to 90%, with the 95% confidence interval ranging from 50% to 99.5% (Figure 5k). These probabilities as well as the width of the confidence intervals exhibit regional variability (Table 1), with Southeast Asia emerging as a region with an elevated likelihood of experiencing record-breaking TW_{\max} during a strong El Niño (Figures 5m and Table 1).

4. Summary and Discussion

This study establishes the potential for dynamically based predictions of the annual maximum of daily maximum wet-bulb temperatures (TW_{\max}) across tropical land areas with an average lead time of about 5 months. This predictability arises from two facts in tropical atmosphere-ocean dynamics: (a) TW_{\max} over tropical land is

closely coupled to free tropospheric temperature through deep convection and tropical wave dynamics, and (b) the free tropospheric temperature is determined by the warmest SSTs, which typically reach their peak around 5 months after the peak of an El Niño event.

By using the Oceanic Niño Index (ONI) as a predictor and accounting for the warming trend through a “year” variable, our multiple linear regression model effectively explains a substantial portion—80%—of the variability in tropical land mean TW_{max} . Although the model's performance varies across regions, it demonstrates promising skill, especially in the deep tropics (Figures 3b–3d, Figure 4a). Both warming trends and ENSO have contributed significantly to the variability in TW_{max} , and our analysis shows that the cumulative warming effect since 1980 is comparable to that of an exceptionally strong El Niño.

We forecasted TW_{max} for the year 2024 assuming knowledge of the December ONI of 2023 and estimated the probability of setting new TW_{max} records in 2024. The strength of an El Niño event significantly influences the probability of breaking TW_{max} records. The tropical mean and regional variations in these probabilities are detailed in Figures 5k–5o and Table 1.

Caution should be taken when applying this model to time periods or regions beyond those used in this study. First, representing warming with the “year” vector assumes a constant long-term rate of change in TW_{max} over time, an assumption that should be modified when applied to periods of nonlinear anthropogenic warming. Second, the spatial heterogeneity in the goodness of fit (Figure 4a) suggests other factors at play as discussed in Text S2 in Supporting Information S1. Third, the timing of TW_{max} varies across different regions. Thus, enhancing the model by incorporating additional information from various ONI months is a logical step forward.

Although TW may not be the most precise metric for evaluating heat stress (Baldwin et al., 2023; Lu & Romps, 2023), the methodology developed in this work has the potential to be adapted to temperature and Heat Index, which are influenced by SST through similar dynamics (Byrne, 2021; Chiang & Sobel, 2002).

Finally, this study calls for increased efforts to enhance the accuracy of predictions of ENSO-induced free-tropospheric temperature variations. Improved predictions for free-tropospheric temperatures, such as T_{500} , could benefit projections of extreme heat stress across tropical continents, as illustrated by the close correlation between the two in Figure 1a. Note that the predictive model proposed in this study does not rely on forecasting future ENSO events; it leverages only the current ENSO state. This model's predictive skill originates from the time lag between tropical tropospheric temperatures and ENSO variability. That said, advances in ENSO forecasting could further extend the lead times at which accurate TW_{max} predictions become feasible.

Data Availability Statement

The Oceanic Niño Index (ONI) is provided by National Oceanic and Atmospheric Administration's Climate Prediction Center and is available here: https://origin.cpc.ncep.noaa.gov/products/analysis_monitoring/enso-stuff/ONI_v5.php. The ERA5 hourly data on pressure levels and single levels from 1979 to present are downloaded from the Copernicus Climate Change Service Climate Data Store (<https://cds.climate.copernicus.eu>). The Hadley Center Sea Ice and Sea Surface Temperature data set (HadISST) is downloaded from <https://www.metoffice.gov.uk/hadobs/hadisst/>.

References

- Arblaster, J. M., & Alexander, L. V. (2012). The impact of the El Niño–Southern Oscillation on maximum temperature extremes. *Geophysical Research Letters*, 39(20). <https://doi.org/10.1029/2012gl053409>
- Baldwin, J. W., Benmarhnia, T., Ebi, K. L., Jay, O., Lutsko, N. J., & Vanos, J. K. (2023). Humidity's role in heat-related health outcomes: A heated debate. *Environmental Health Perspectives*, 131(5), 055001. <https://doi.org/10.1289/ehp11807>
- Brown, R. G., & Bretherton, C. S. (1997). A test of the strict quasi-equilibrium theory on long time and space scales. *Journal of the Atmospheric Sciences*, 54(5), 624–638. [https://doi.org/10.1175/1520-0469\(1997\)054<0624:atotsq>2.0.co;2](https://doi.org/10.1175/1520-0469(1997)054<0624:atotsq>2.0.co;2)
- Buzan, J. R., & Huber, M. (2020). Moist heat stress on a hotter earth. *Annual Review of Earth and Planetary Sciences*, 48(1), 623–655. <https://doi.org/10.1146/annurev-earth-053018-060100>
- Byrne, M. P. (2021). Amplified warming of extreme temperatures over tropical land. *Nature Geoscience*, 14(11), 837–841. <https://doi.org/10.1038/s41561-021-00828-8>
- Chiang, J. C., & Lintner, B. R. (2005). Mechanisms of remote tropical surface warming during El Niño. *Journal of Climate*, 18(20), 4130–4149. <https://doi.org/10.1175/jcli3529.1>
- Chiang, J. C., & Sobel, A. H. (2002). Tropical tropospheric temperature variations caused by ENSO and their influence on the remote tropical climate. *Journal of Climate*, 15(18), 2616–2631. [https://doi.org/10.1175/1520-0442\(2002\)015<2616:ttvcb>2.0.co;2](https://doi.org/10.1175/1520-0442(2002)015<2616:ttvcb>2.0.co;2)

Acknowledgments

Y.Z. acknowledges the support from the Miller Institute for Basic Research in Science at the University of California, Berkeley. This research was partially supported by the Director, Office of Science, Office of Biological and Environmental Research of the U.S. Department of Energy as part of the Regional and Global Model Analysis program area within the Earth and Environmental Systems Modeling Program under Contract No. DE-AC02-05CH11231 and used resources of the National Energy Research Scientific Computing Center (NERSC), also supported by the Office of Science of the U.S. Department of Energy, under Contract No. DE-AC02-05CH11231. The authors thank the Statistical Consulting provided by the Department of Statistics at the University of California Berkeley, represented by Hyunsuk Kim and James B. Brown, and Mark Risser for their valuable feedback on the statistical approaches.

- ECMWF, S. P. (2014). *In ifs documentation cy40r1 part iv: Physical processes* (pp. 111–113). ECMWF.
- Fueglistaler, S. (2019). Observational evidence for two modes of coupling between sea surface temperatures, tropospheric temperature profile, and shortwave cloud radiative effect in the tropics. *Geophysical Research Letters*, *46*(16), 9890–9898. <https://doi.org/10.1029/2019gl083990>
- Gill, A. E. (1980). Some simple solutions for heat-induced tropical circulation. *Quarterly Journal of the Royal Meteorological Society*, *106*(449), 447–462. <https://doi.org/10.1002/qj.49710644905>
- Held, I. M., & Hou, A. Y. (1980). Nonlinear axially symmetric circulations in a nearly inviscid atmosphere. *Journal of the Atmospheric Sciences*, *37*(3), 515–533. [https://doi.org/10.1175/1520-0469\(1980\)037<0515:nascia>2.0.co;2](https://doi.org/10.1175/1520-0469(1980)037<0515:nascia>2.0.co;2)
- Hersbach, H., Bell, B., Berrisford, P., Hirahara, S., Horányi, A., Muñoz-Sabater, J., et al. (2020). The era5 global reanalysis. *Quarterly Journal of the Royal Meteorological Society*, *146*(730), 1999–2049. <https://doi.org/10.1002/qj.3803>
- Hogikyan, A., Resplandy, L., & Fueglistaler, S. (2022). Cause of the intense tropics-wide tropospheric warming in response to El Niño. *Journal of Climate*, *35*(10), 2933–2944. <https://doi.org/10.1175/jcli-d-21-0728.1>
- Ivanovich, C., Anderson, W., Horton, R., Raymond, C., & Sobel, A. (2022). The influence of intraseasonal oscillations on humid heat in the Persian gulf and South Asia. *Journal of Climate*, *35*(13), 4309–4329. <https://doi.org/10.1175/jcli-d-21-0488.1>
- Klein, S. A., Soden, B. J., & Lau, N.-C. (1999). Remote sea surface temperature variations during ENSO: Evidence for a tropical atmospheric bridge. *Journal of Climate*, *12*(4), 917–932. [https://doi.org/10.1175/1520-0442\(1999\)012<0917:rsstvd>2.0.co;2](https://doi.org/10.1175/1520-0442(1999)012<0917:rsstvd>2.0.co;2)
- Kong, Q., & Huber, M. (2023). Regimes of soil moisture-wet bulb temperature coupling with relevance to moist heat stress. *Journal of Climate*, *36*(22), 1–45. <https://doi.org/10.1175/jcli-d-23-0132.1>
- Lu, Y.-C., & Romps, D. M. (2023). Is a wet-bulb temperature of 35° c the correct threshold for human survivability? *Environmental Research Letters*, *18*(9), 094021. <https://doi.org/10.1088/1748-9326/ace83c>
- Matsumo, T. (1966). Quasi-geostrophic motions in the equatorial area. *Journal of the Meteorological Society of Japan. Ser. II*, *44*(1), 25–43. https://doi.org/10.2151/jmsj1965.44.1_25
- Pal, J. S., & Eltahir, E. A. (2001). Pathways relating soil moisture conditions to future summer rainfall within a model of the land–atmosphere system. *Journal of Climate*, *14*(6), 1227–1242. [https://doi.org/10.1175/1520-0442\(2001\)014<1227:prsmct>2.0.co;2](https://doi.org/10.1175/1520-0442(2001)014<1227:prsmct>2.0.co;2)
- Pan, Y. H., & Oort, A. H. (1983). Global climate variations connected with sea surface temperature anomalies in the eastern equatorial pacific ocean for the 1958–73 period. *Monthly Weather Review*, *111*(6), 1244–1258. [https://doi.org/10.1175/1520-0493\(1983\)111<1244:gevcws>2.0.co;2](https://doi.org/10.1175/1520-0493(1983)111<1244:gevcws>2.0.co;2)
- Parkes, B., Buzan, J. R., & Huber, M. (2022). Heat stress in Africa under high intensity climate change. *International Journal of Biometeorology*, *66*(8), 1531–1545. <https://doi.org/10.1007/s00484-022-02295-1>
- Raymond, C., Matthews, T., & Horton, R. M. (2020). The emergence of heat and humidity too severe for human tolerance. *Science Advances*, *6*(19), eaaw1838. <https://doi.org/10.1126/sciadv.aaw1838>
- Raymond, C., Matthews, T., Horton, R. M., Fischer, E. M., Fueglistaler, S., Ivanovich, C., et al. (2021). On the controlling factors for globally extreme humid heat. *Geophysical Research Letters*, *48*(23), e2021GL096082. <https://doi.org/10.1029/2021gl096082>
- Rayner, N., Parker, D. E., Horton, E., Folland, C. K., Alexander, L. V., Rowell, D., et al. (2003). Global analyses of sea surface temperature, sea ice, and night marine air temperature since the late nineteenth century. *Journal of Geophysical Research*, *108*(D14). <https://doi.org/10.1029/2002jd002670>
- Revadekar, J., Kothawale, D., & Rupa Kumar, K. (2009). Role of El Niño/La Niña in temperature extremes over India. *International Journal of Climatolgy: A Journal of the Royal Meteorological Society*, *29*(14), 2121–2129. <https://doi.org/10.1002/joc.1851>
- Rogers, C. D., Ting, M., Li, C., Kornhuber, K., Coffel, E. D., Horton, R. M., et al. (2021). Recent increases in exposure to extreme humid-heat events disproportionately affect populated regions. *Geophysical Research Letters*, *48*(19), e2021GL094183. <https://doi.org/10.1029/2021gl094183>
- Sherwood, S. C., & Huber, M. (2010). An adaptability limit to climate change due to heat stress. *Proceedings of the National Academy of Sciences*, *107*(21), 9552–9555. <https://doi.org/10.1073/pnas.0913352107>
- Sobel, A. H., Held, I. M., & Bretherton, C. S. (2002). The ENSO signal in tropical tropospheric temperature. *Journal of Climate*, *15*(18), 2702–2706. [https://doi.org/10.1175/1520-0442\(2002\)015<2702:tesitt>2.0.co;2](https://doi.org/10.1175/1520-0442(2002)015<2702:tesitt>2.0.co;2)
- Speizer, S., Raymond, C., Ivanovich, C., & Horton, R. M. (2022). Concentrated and intensifying humid heat extremes in the IPCC ar6 regions. *Geophysical Research Letters*, *49*(5), e2021GL097261. <https://doi.org/10.1029/2021gl097261>
- Su, H., Neelin, J. D., & Meyerson, J. E. (2005). Mechanisms for lagged atmospheric response to ENSO SST forcing. *Journal of Climate*, *18*(20), 4195–4215. <https://doi.org/10.1175/jcli3514.1>
- Thirumalai, K., Di Nezio, P. N., Okumura, Y., & Deser, C. (2017). Extreme temperatures in Southeast Asia caused by El Niño and worsened by global warming. *Nature Communications*, *8*(1), 15531. <https://doi.org/10.1038/ncomms15531>
- Webster, P. J., & Yang, S. (1992). Monsoon and ENSO: Selectively interactive systems. *Quarterly Journal of the Royal Meteorological Society*, *118*(507), 877–926. <https://doi.org/10.1256/smsqj.50704>
- Xie, S.-P., Hu, K., Hafner, J., Tokinaga, H., Du, Y., Huang, G., & Sampe, T. (2009). Indian ocean capacitor effect on indo–western pacific climate during the summer following El Niño. *Journal of Climate*, *22*(3), 730–747. <https://doi.org/10.1175/2008jcli2544.1>
- Yulaeva, E., & Wallace, J. M. (1994). The signature of ENSO in global temperature and precipitation fields derived from the microwave sounding unit. *Journal of Climate*, *7*(11), 1719–1736. [https://doi.org/10.1175/1520-0442\(1994\)007<1719:tsoeig>2.0.co;2](https://doi.org/10.1175/1520-0442(1994)007<1719:tsoeig>2.0.co;2)
- Zhang, Y., & Fueglistaler, S. (2020). How tropical convection couples high moist static energy over land and ocean. *Geophysical Research Letters*, *47*(2), e2019GL086387. <https://doi.org/10.1029/2019gl086387>
- Zhang, Y., Held, I., & Fueglistaler, S. (2021). Projections of tropical heat stress constrained by atmospheric dynamics. *Nature Geoscience*, *14*(3), 133–137. <https://doi.org/10.1038/s41561-021-00695-3>

Supporting Information for “Forecasting Tropical Annual Maximum Wet-Bulb Temperatures Months in Advance from the Current State of El Niño”

Yi Zhang^{1,2}, William R. Boos^{1,3}, Isaac Held⁴, Christopher J. Paciorek⁵,

Stephan Fueglistaler^{4,6}

¹Department of Earth and Planetary Science, University of California, Berkeley, CA 94720

²Miller Institute for Basic Research in Science, University of California, Berkeley, CA 94720

³Climate and Ecosystem Sciences Division, Lawrence Berkeley National Laboratory, CA 94720

⁴Program in Atmospheric and Oceanic Sciences, Princeton University, Princeton, NJ 08540

⁵Department of Statistics, University of California, Berkeley, CA 94720

⁶Department of Geosciences, Princeton University, Princeton, NJ 08540

Contents of this file

1. Text S1 to S5

2. Figures S1 to S4

Text S1. Fitting generalized extreme value distributions

The generalized extreme value (GEV) distribution is represented by the probability density function:

$$f(x; \mu, \sigma, \xi) = \begin{cases} \exp\left(-\left[1 + \xi\left(\frac{x-\mu}{\sigma}\right)\right]^{-1/\xi}\right) \left[1 + \xi\left(\frac{x-\mu}{\sigma}\right)\right]^{-(\frac{1}{\xi}+1)} \frac{1}{\sigma}, & \text{for } \xi \neq 0, \\ \exp\left(-\exp\left(\frac{-(x-\mu)}{\sigma}\right)\right) \exp\left(\frac{-(x-\mu)}{\sigma}\right) \frac{1}{\sigma}, & \text{for } \xi = 0. \end{cases} \quad (1)$$

In our model, the location parameter, μ , is defined as a linear combination of the year (t) and the Oceanic Niño Index from the preceding December (ONI_{t-1}):

$$\mu = \beta_0 + \beta_1 t + \beta_2 \text{ONI}_{t-1} \quad (2)$$

Thus, the log-likelihood function, given the data, can be expressed as:

$$L(\beta_0, \beta_1, \beta_2, \sigma, \xi | \text{TW}_{\max,1}, \dots, \text{TW}_{\max,n}, t_1, \dots, t_n, \text{ONI}_0, \dots, \text{ONI}_{t-1})$$

$$= \begin{cases} -n \ln \sigma - \left(1 + \frac{1}{\xi}\right) \sum_{t=1}^n \ln\left(1 + \xi \frac{\text{TW}_{\max} - \beta_0 - \beta_1 t - \beta_2 \text{ONI}_{t-1}}{\sigma}\right) - \sum_{t=1}^n \left(1 + \xi \frac{\text{TW}_{\max} - \beta_0 - \beta_1 t - \beta_2 \text{ONI}_{t-1}}{\sigma}\right)^{-\frac{1}{\xi}} & \text{if } \xi \neq 0 \\ -n \ln \sigma - \sum_{t=1}^n \frac{\text{TW}_{\max} - \beta_0 - \beta_1 t - \beta_2 \text{ONI}_{t-1}}{\sigma} - \sum_{t=1}^n \exp\left(-\frac{\text{TW}_{\max} - \beta_0 - \beta_1 t - \beta_2 \text{ONI}_{t-1}}{\sigma}\right) & \text{if } \xi = 0 \end{cases}$$

To obtain optimal parameter values, the negative log-likelihood ($-L$) is minimized using the “minimize” function from Python’s “scipy” package. The estimated $\hat{\beta}$ values derived this way, as well as the Mean Squared Error (MSE), are quite similar to those from a standard multiple linear regression (not shown).

Text S2. Spatial patterns of the regression coefficient with regard to warming

There are two potential causes of the spatial pattern in the coefficient of warming ($\hat{\beta}_1^*$): the uneven response of free-tropospheric temperatures to localized convective heating, and the influence of local land surface conditions.

To assess the former, we applied the multiple linear regression from Eq. (1) to the annual mean 500-hPa temperature (T_{500}) to detect any similarities with the spatial patterns of regression coefficients seen for TW_{\max} . Both warming (Figure S2b) and El Niños (Figure S2c) positively affect annual mean T_{500} across tropical continents. While there are discernible spatial patterns in the standardized regression coefficients for warming’s impact on T_{500} , they remain positive and don’t align with the patterns observed in $\hat{\beta}_1^*$ (Figure 4b). The negative $\hat{\beta}_1^*$ values for TW_{\max} thus might not be tied to T_{500} ; however, relying on the annual mean T_{500} could potentially overlook higher frequency T_{500} variability associated with days on which TW_{\max} occurs.

To explore the other possible cause of the spatial pattern in the standardized coefficient of warming—local land surface conditions—we analyzed local annual mean 2-m air temperature (T_s) and specific humidity (q_s) trends. Most tropical land regions show predominantly positive T_s trends (Figure S1a). In contrast, q_s trends are more spatially varied. Areas with negative $\hat{\beta}_1^*$ values, notably parts of Africa, South America, and Australia, reveal significant drying trends in the annual mean q_s (Figure S1b). This drying offsets T_s warming, and the ensuing annual mean moist static energy trends (Figure S1c) closely mirror the distribution of $\hat{\beta}_1^*$. This indicates a potential link between local drying and negative TW_{\max} trends. In any case, interpreting q_s trends over tropical continents requires caution as these regions lack abundant long-term in-situ measurements.

To summarize, it is very likely that local land surface conditions play a role in the spatial inhomogeneity of $\hat{\beta}_1^*$. This could be through land use change and soil moisture-

TW coupling. It is unclear whether TW_{\max} over regions of negative are $\hat{\beta}_1^*$ tightly coupled to T_{500} from the current analysis and future research is warranted.

Text S3. Cross-validation of the regression model

Before generating predictions with the multiple linear regression model, we evaluate its predictive performance through leave-one-out cross-validation and walk-forward validation.

The leave-one-out cross-validation results in a 9.4% increase in the Root Mean Squared Error (RMSE) for the tropical mean. Similarly, the increase in RMSE ranges from 8.9% to 9.7% for each of the four focus regions, as shown in Table 1.

The walk-forward validation can be regarded as a simulation of real-time forecasting. The model is initially fitted on a 20-year segment of the time series data (from 1980 to 2003 with 1983-1984 and 1992-1993 removed). After fitting, the model is tested on the year immediately following the training set. This process repeats by “walking forward” in time - each time, the model is re-trained on a segment that includes one more year of data and then tested on the subsequent year. The results are presented in Figure S6 and Table 1. The RMSE for the last 19 data points shows a 7.1% increase for the tropical mean and ranges from 17.6% to 20.1% for the four regions.

These moderate increases in RMSE from both the leave-one-out cross-validation and walk-forward validation suggest that the model is not seriously overfit. If there is a substantial increase in the RMSE when certain samples are omitted from the training set during cross-validation, this suggests the model may struggle with generalizing to unseen data, rendering it potentially unsuitable for predictive purposes. Moderate increases in

the RMSE suggest that the model maintains a certain level of robustness and reliability in its predictions of unseen data.

Text S4. Confidence intervals and prediction intervals

The confidence interval quantifies the range of uncertainty about a population parameter, in this case, $\hat{\text{TW}}_{\max}$. The prediction interval quantifies the range within which we expect a single new TW_{\max} observation to fall. This prediction interval takes into account not only the uncertainty in estimating the mean of predicted TW_{\max} but also the year-to-year variability in individual TW_{\max} observations. Consequently, prediction intervals are wider and are more relevant when using this model for forecasting TW_{\max} in a forthcoming year.

The 95% confidence interval of the predicted mean $\hat{\text{TW}}_{\max}$ is calculated as:

$$\hat{\text{TW}}_{\max} \pm t_{0.025,36} \text{se}(\hat{\text{TW}}_{\max}) \quad (3)$$

where the t value of a two-sided significance level of 0.05 with 36 degrees of freedom is 2.028. The 95% prediction interval is given by:

$$\hat{\text{TW}}_{\max} \pm t_{0.025,36} \sqrt{\text{MSE} + \text{se}(\hat{\text{TW}}_{\max})^2}, \quad (4)$$

where the standard error of fit at $\mathbf{x}_{\mathbf{p}} = (1, 2024, \text{ONI}_{\text{Dec},2023})^T$ is determined by

$$\text{se}(\hat{\text{TW}}_{\max})^2 = \text{MSE} \mathbf{x}_{\mathbf{p}}^T (X^T X)^{-1} \mathbf{x}_{\mathbf{p}} \quad (5)$$

with MSE being the mean squared error and X being the 39×3 regressor matrix:

$$X = \begin{bmatrix} 1 & 1980 & \text{ONI}_{\text{Dec},1979} \\ 1 & 1981 & \text{ONI}_{\text{Dec},1980} \\ 1 & 1982 & \text{ONI}_{\text{Dec},1981} \\ 1 & 1985 & \text{ONI}_{\text{Dec},1984} \\ \vdots & \vdots & \vdots \\ 1 & 1991 & \text{ONI}_{\text{Dec},1990} \\ 1 & 1994 & \text{ONI}_{\text{Dec},1993} \\ \vdots & \vdots & \vdots \\ 1 & 2022 & \text{ONI}_{\text{Dec},2021} \end{bmatrix}. \quad (6)$$

MSE is calculated following

$$\text{MSE} = \frac{1}{n - k - 1} \sum_{i=1}^n (y_i - \hat{y}_i)^2, \quad (7)$$

where n is the number of samples and $k = 2$ is the number of independent variables.

Text S5. Confidence intervals for the exceedance probability

We calculate the confidence intervals of the probability by bootstrapping the original 39 data points and associated covariate values (a nonparametric bootstrap). For each of the 9999 bootstrap replicates, we estimate the probability of exceeding the previous record using the multiple linear regression model. Specifically, we assume that the predicted TW_{max} at each $\mathbf{x}_p = (1, 2024, \text{ONI}_{\text{Dec},2023})^T$ follows a Gaussian distribution centering at the predicted mean given by Equation (6) with a standard deviation equalling the root mean squared error (RMSE). For each $\text{ONI}_{\text{Dec},2023}$ value, we then compute the area under this Gaussian distribution when the predicted TW_{max} exceeds the highest record, resulting in the probability of a new TW_{max} record being set for this replicate. Given the potential skewness of the probability distribution when the central estimate approaches 0 or 1, we employ the bias-corrected and accelerated (BCa) method for bootstrap confidence intervals. The BCa bootstrap analysis is conducted using the R “boot” package.

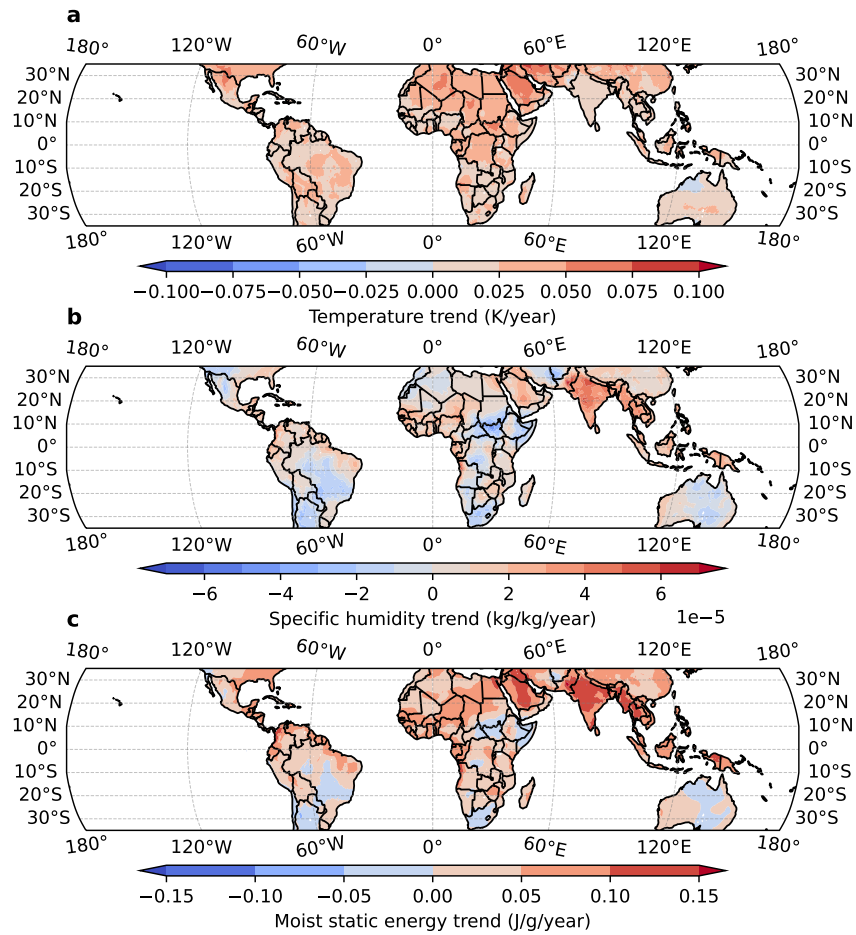


Figure S1. Linear trends of annual-mean 2-m air temperature (a), specific humidity (b), and moist static energy (c) from 1979 to 2022 according to ERA5.

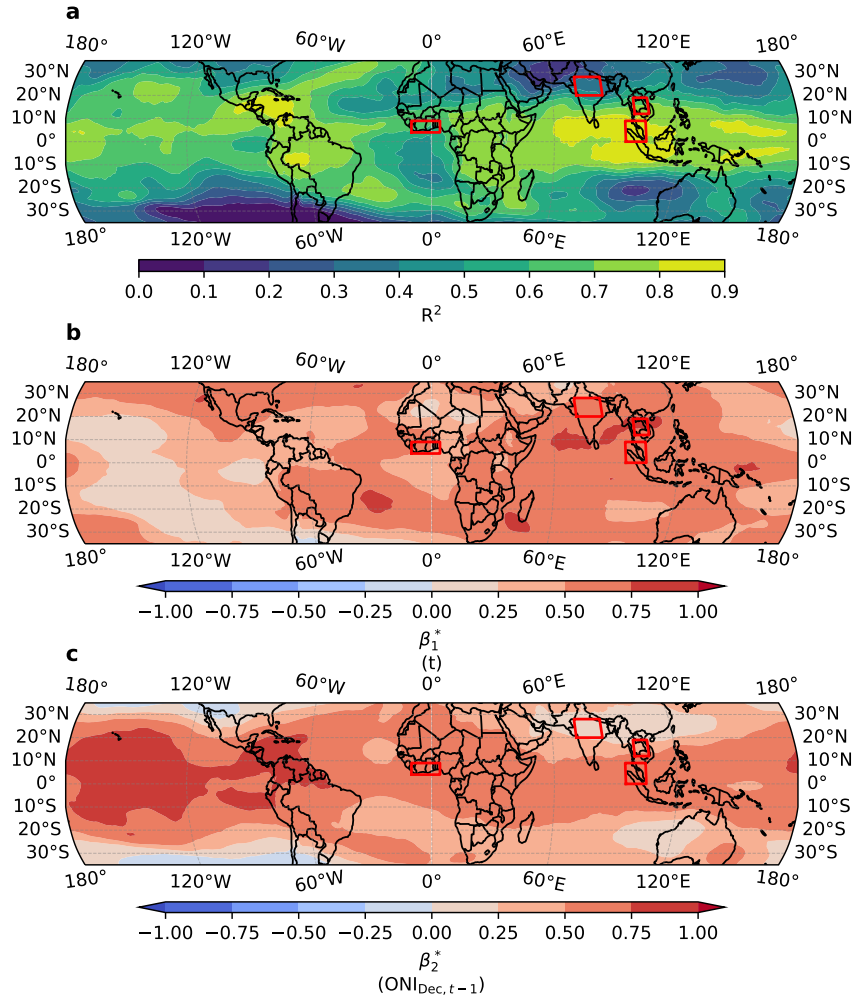


Figure S2. Results of fitting the same model in Eq. (4) but with the annual mean 500-hPa temperature (T_{500}) as the dependent variable. **a**, R^2 . **b**, Standardized regression coefficient of constant warming. **c**, Standardized regression coefficient of ENSO variability.

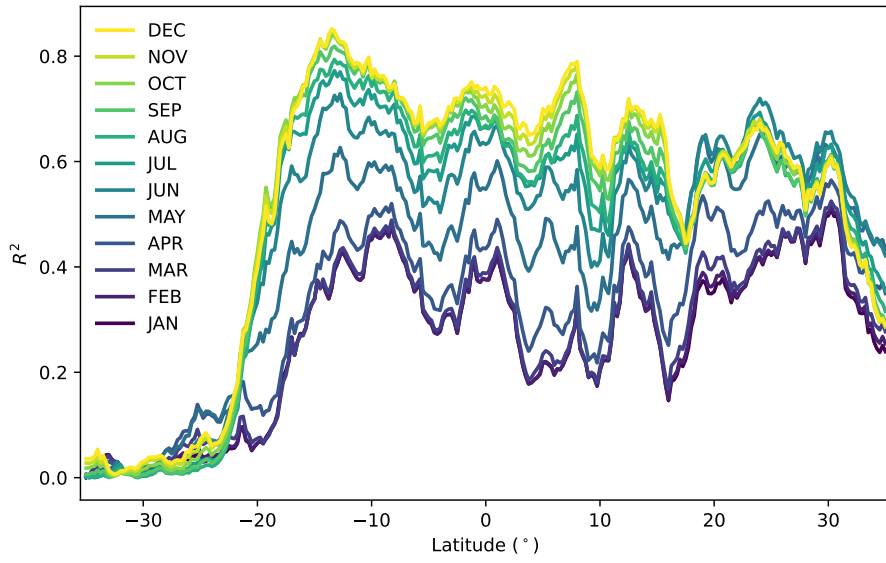


Figure S3. R^2 of the model in Eq. (4) fitted to zonal-land-mean TW_{max} using ONI of each month from preceding years.

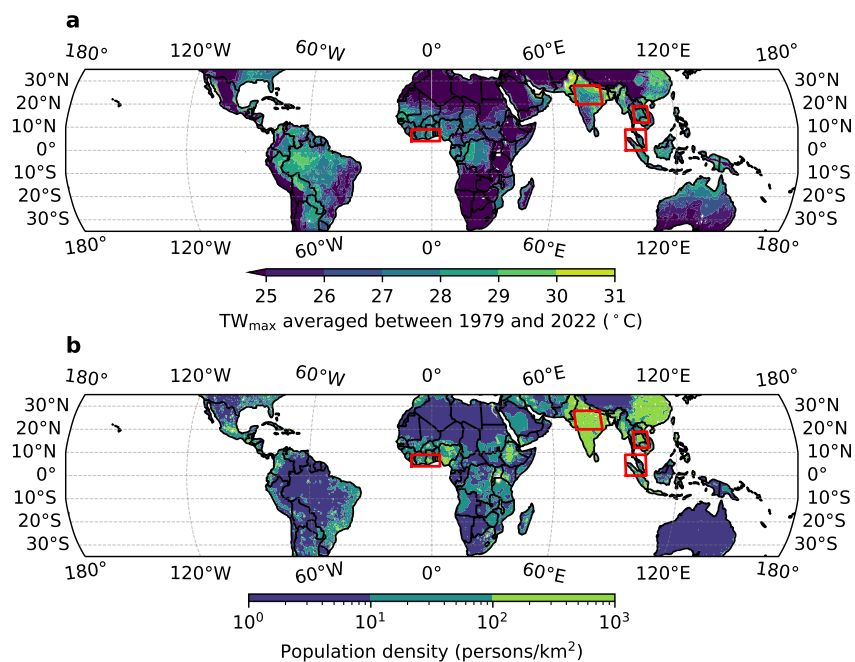


Figure S4. a, Climatology of the annual maximum TW (TW_{max}) between 1979 and 2022. The color scale only distinguishes values greater than $25^{\circ}C$. b, Population density map acquired from https://neo.gsfc.nasa.gov/view.php?datasetId=SEDAC_POP.

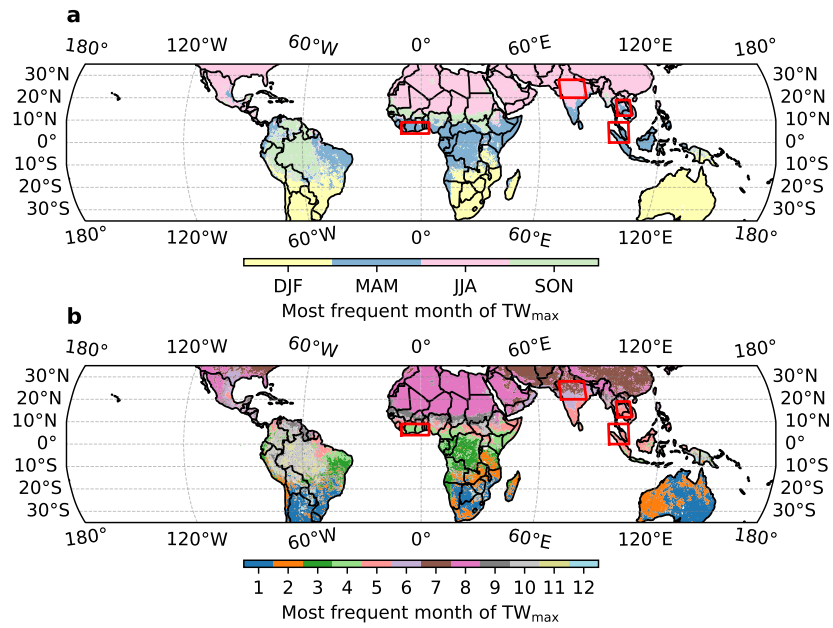


Figure S5. The most common month for the occurrence of annual maximum TW for each location. Groupings of three months (DJF, MAM, JJA, SON) are shown in **b**, along with individual months.

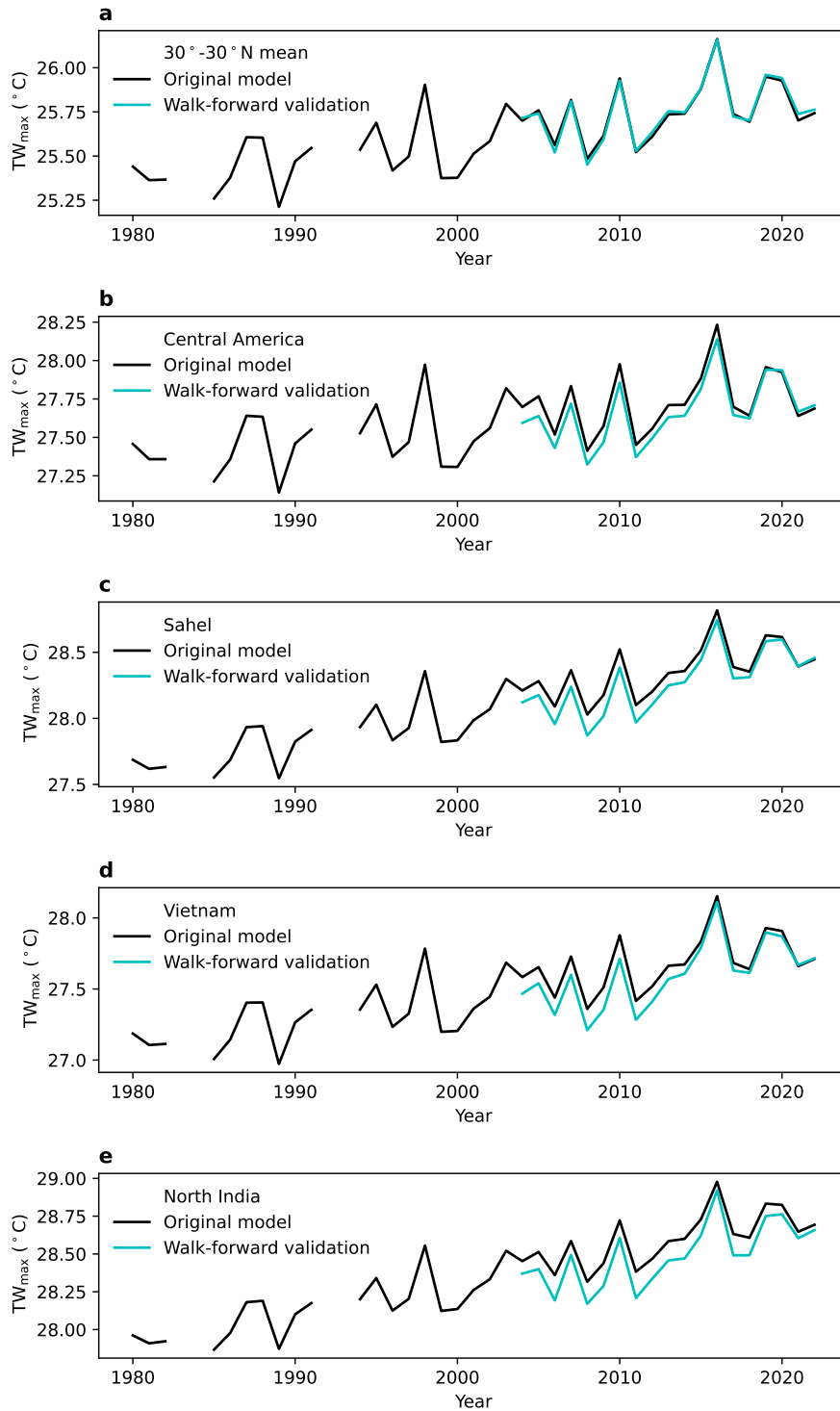


Figure S6. Time series of predicted TW_{max} from the original model with all the 39 data points and that from walk-forward validation for the 30°S-30°N land average (**a**) and for each of the four defined regions of interest (**b-e**). The initial training set contains the first 20 data points. The missing points are the post-volcanic eruption years.

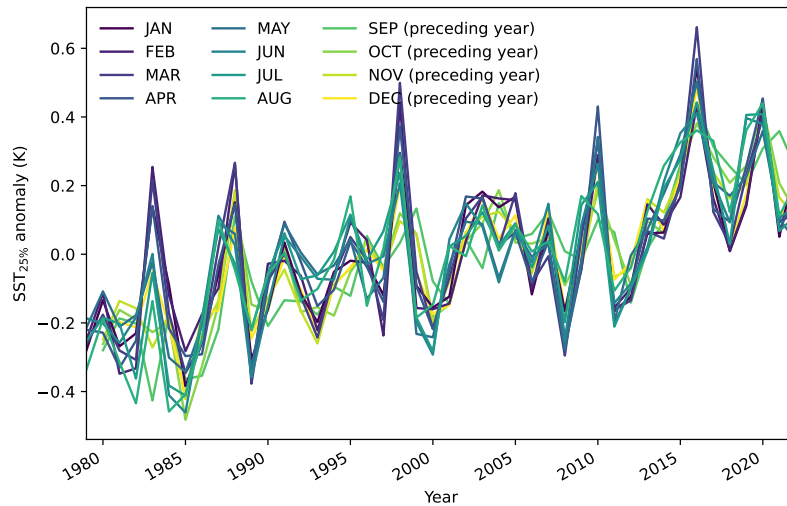


Figure S7. Top 25% mean SST between 30°S and 30°N for each month of year has similar interannual variability. The average of the top 25% of monthly mean SST for each month is calculated and the average of all years for each month is subtracted to emphasize the anomalies. To align with the ENSO cycle, SST_{25%} anomalies for the months of September to December for the preceding calendar year are shown, thereby initiating the annual cycle from September.